PROCEEDINGS OF SPIE

SPIEDigitalLibrary.org/conference-proceedings-of-spie

A new metrology technique for defect inspection via coherent Fourier scatterometry using orbital angular momentum beams

Wang, Bin, Tanksalvala, Michael, Zhang, Zhe, Esashi, Yuka, Jenkins, Nicholas, et al.

Bin Wang, Michael Tanksalvala, Zhe Zhang, Yuka Esashi, Nicholas W. Jenkins, Margaret M. Murnane, Henry C. Kapteyn, Chen-Ting Liao, "A new metrology technique for defect inspection via coherent Fourier scatterometry using orbital angular momentum beams," Proc. SPIE 11611, Metrology, Inspection, and Process Control for Semiconductor Manufacturing XXXV, 116110L (22 February 2021); doi: 10.1117/12.2584728

SPIE.

Event: SPIE Advanced Lithography, 2021, Online Only

A new metrology technique for defect inspection via coherent Fourier scatterometry using orbital angular momentum beams

Bin Wang[a,b], Michael Tanksalvala[a,b], Zhe Zhang[a,b,c], Yuka Esashi[a,b], Nicholas W. Jenkins[a,b], Margaret M. Murnane[a,b], Henry C. Kapteyn[a,b,d], Chen-Ting Liao[a,b]
[a]JILA, University of Colorado and NIST, 440UCB, Boulder, Colorado80309, USA; [b]STROBE Science and Technology Center, JILA and Department of Physics, University of Colorado, Boulder, Colorado 80309, USA; [c]MOE Key Laboratory of Advanced Microstructural Materials, Insititute of Precision Optical Engineering, School of Physics Science and Engineering, Tongji University, Shanghai 200092, China; [d]KMLabs Inc., 4775 Walnut St. Building 102, Boulder, Colorado 80301, USA

ABSTRACT

Coherent Fourier scatterometry (CFS) via laser beams with a Gaussian spatial profile is routinely used as an in-line inspection tool to detect defects on, for example, lithographic substrates, masks, reticles, and wafers. New metrology techniques that enable high-throughput, high-sensitivity, and in-line inspection are critically in need for next-generation high-volume manufacturing including those based on extreme ultraviolet (EUV) lithography. Here, a set of novel defect inspection techniques are proposed and investigated numerically [Wang *et al.,* Opt. Express 29, 3342 (2021)], which are based on bright-field CFS using coherent beams that carry orbital angular momentum (OAM). One of our proposed methods, the differential OAM CFS, is particularly unique because it does not require a pre-established database for comparison in the case of regularly patterned structures with reflection symmetry such as 1D and 2D grating structures. We studied the performance of these metrology techniques on both amplitude and phase defects. We demonstrated their superior advantages, which shows up to an order of magnitude higher in signal-to-noise ratio over the conventional Gaussian beam CFS. These metrology techniques will enable higher sensitivity and robustness for in-line nanoscale defect inspection. In general, our concept could benefit EUV and x-ray scatterometry as well.

Keywords: defect inspection, coherent Fourier scatterometry, CFS, orbital angular momentum, OAM,

1. INTRODUCTION

In semiconductor manufacturing, defect inspection on wafers and masks is routinely accomplished by first using in-line optical scatterometry techniques to detect rough locations, and then using other off-line instruments, such as atomic force microscopy and scanning electron microscopy, to extract defect details, such as location, shape, and composition. However, locating and classifying defects with in-line measurements is highly desirable to avoid the need to remove the wafer from the fabrication line. Coherent Fourier scatterometry (CFS), as an in-line metrology technique, was originally developed to characterize grating structures and has also been demonstrated to have high sensitivity for nanoparticle detection on silicon, glass, and plastic substrates [1,2]. In CFS, one scans a tightly focused coherent laser beam across a sample and records far-field diffraction patterns, and any change in the far-field patterns indicate the existence of defects. CFS can be implemented in a dark-field or bright-field modality. Dark-field CFS techniques block the specular reflection and capture only the remaining high-angle scattered light. They allow for sensitive detection of deep sub-wavelength scale defects, but will damage the sample because the incident illumination power must be high enough to achieve the threshold signal-to-noise ratio (SNR) for confident detection. In contrast, bright-field CFS techniques, which collect both the specular reflection and high-angle scattering, require much lower incident power and do not suffer from the radiation damage problem. However, the weak scattering and low SNR limits the sensitivity, such that sub-100 nm defects are difficult to detect using visible light alone.

Conventional CFS inspection of semiconductor samples uses Gaussian laser beams as illumination. Recently, laser beams carrying orbital angular momentum (OAM) [3] have been demonstrated to possess promising applications in enhanced optical sensing, imaging, and high-bandwidth communication [4-6]. OAM beams have a helix-shaped wavefront and are characterized by an integer quantum number q, called the OAM charge, the sign of which determines the handedness of

Metrology, Inspection, and Process Control for Semiconductor Manufacturing XXXV,
edited by Ofer Adan, John C. Robinson, Proc. of SPIE Vol. 11611, 116110L
 · doi: 10.1117/12.2584728

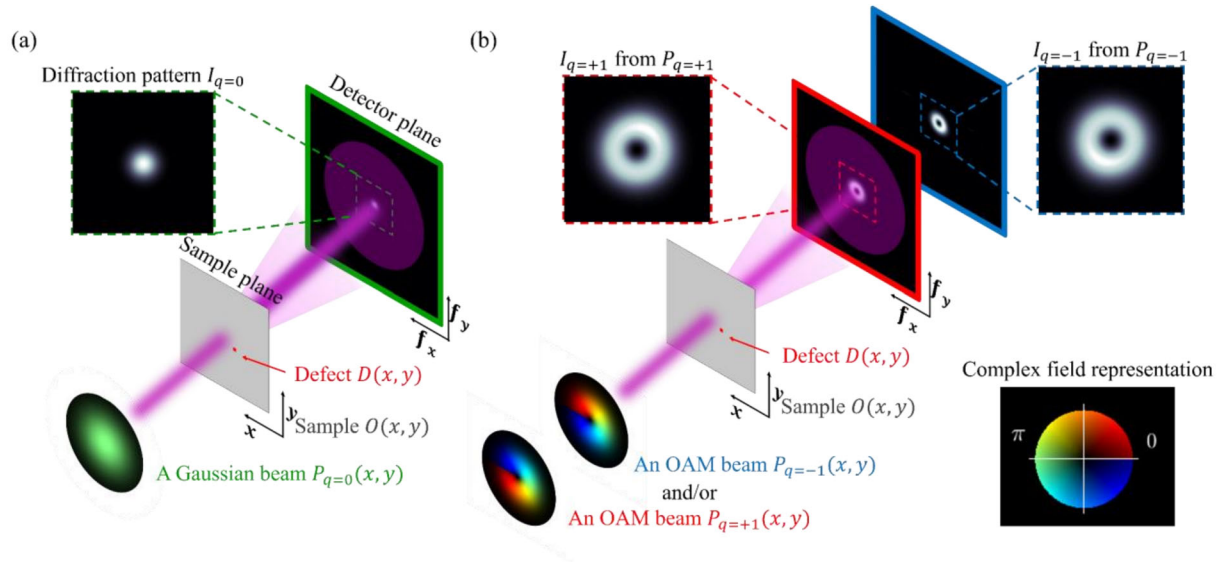

Fig. 1. Schematic of coherent Fourier scatterometry techniques using different illumination beams. (a) Model-based Gaussian CFS. A Gaussian beam illuminates a defect-free sample $O(x,y)$, which is chosen to be a uniform planar substrate for discussion, with a point defect $D(x,y)$, marked in red, and the far-field diffraction patterns, $I_{q=0}$, are recorded on the detector plane. The complex wavefront of the Gaussian beam $P_{q=0}(x,y)$ is plotted with amplitude and phase being represented as brightness and hue, respectively, as shown in the color wheel of the inset. The green dashed box shows the center of the diffraction pattern. (b) Model-based OAM CFS, model-based differential OAM CFS, and model-free OAM CFS. All three techniques share the same experimental setup but differ in data collection and processing. When illuminating with a single OAM beam $P_q(x,y)$ with integer OAM charge $q = +1$ or $q = -1$, the resulting diffraction pattern, I_q, is shown in the red or blue solid boxes, respectively. Note that the diffraction patterns from OAM beams exhibit an obvious asymmetry, which can be leveraged to perform defect inspection. A Gaussian beam can be regarded as a special OAM beam with $q = 0$. All beams share the same complex field representation. This figure is adopted from Ref. [12].

the helical wavefront. The diffraction of an OAM beam from a sample shows characteristics different from that of a Gaussian beam. Moreover, the diffraction patterns of two OAM beams with opposite OAM charges from the same sample show different characteristics. This allows us to perform differential CFS as a powerful metrology technique for defect inspection. Our OAM beam CSF is inspired by structured illumination microscopy, which enhances imaging performance by utilizing illuminations with specifically designed amplitude or phase structures. Recently, simple structured illumination with a binary phase structure was used to enhance the detection of nanoscale grating asymmetry and overlay error [7,8].

Here, we combine bright-field CFS techniques with OAM beams to solve the problem of high-sensitivity and in-line detection of nanoscale defects with minimal radiation damage. The paper is organized as follows: Section 2 introduces the new CFS techniques using OAM beams. In Section 3, the sensitivity enhancement of OAM beam-based CFS is discussed, and two data processing techniques based on the detection of asymmetry in far-field diffraction patterns are proposed. Numerical simulations are conducted to compare the performance of CFS techniques using Gaussian and OAM beams. Finally, we conclude the paper in Section 4.

2. COHERENT FOURIER SCATTEROMETRY TECHNIQUES

2.1 Model-based CFS using a Gaussian beam

In conventional model-based CFS using a Gaussian beam (referred to as model-based Gaussian CFS), a spatially coherent Gaussian beam is scanned across a sample under inspection and the far-field diffraction patterns are recorded. In Fig. 1, the sample, $O(x,y)$ representing either the complex reflectivity or transmissivity, is modeled as the sum of a defect-free sample, $S(x,y)$, and a small additive defect, $D(x,y)$, *i.e.,* $O(x,y) = S(x,y) + D(x,y)$. We focus on cases where the defect-free sample is a uniform substrate, and the defect is a nanoscale particle or contamination. Illuminating with a coherent Gaussian beam, $P_{q=0}(x,y)$, the far-field diffraction patterns can be mathematically written as:

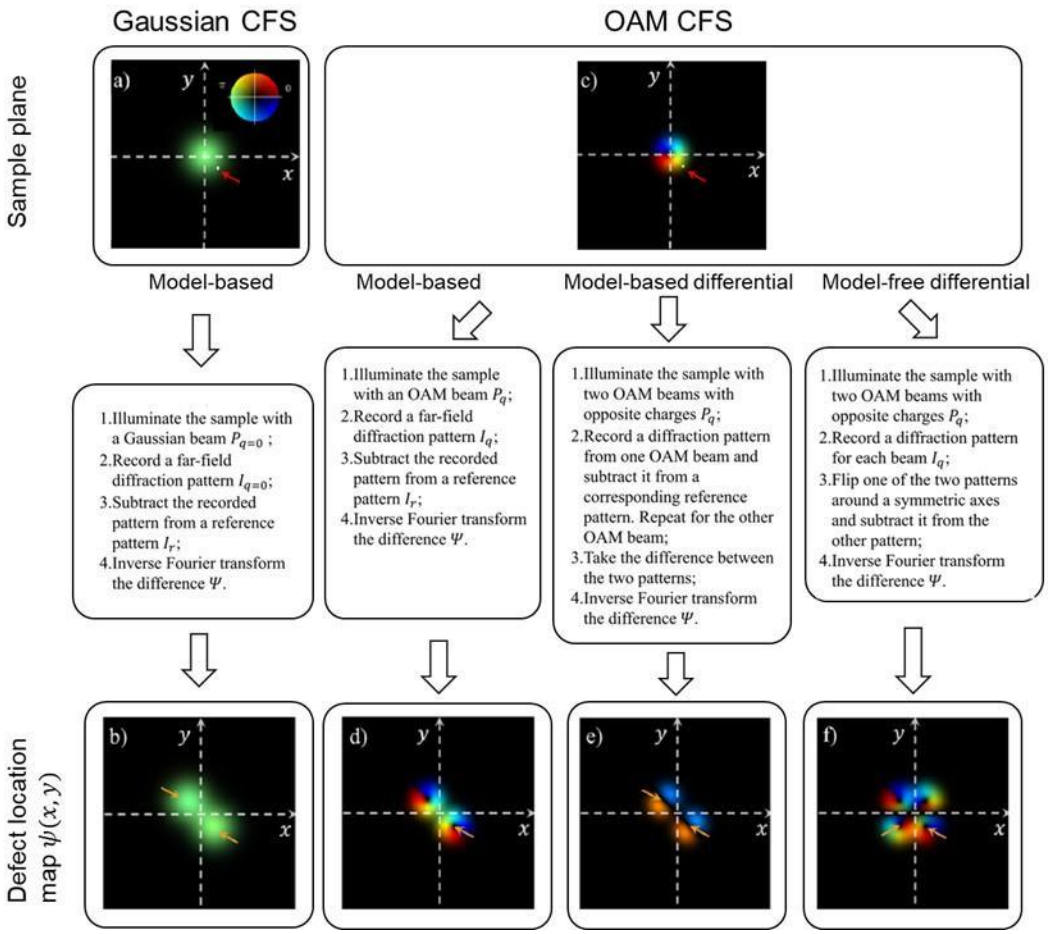

Fig. 2. CFS data recording and processing flow, including conventional Gaussian CFS (first column) and OAM beam-based CSF (second, third, and forth columns). On the sample plane, an illumination incident onto a sample, which is chosen to be a uniform planar substrate for discussion, with a point defect (the white dot pointed by the red arrow) are shown in (a) and (c) for a Gaussian and an OAM beam with $q = 1$, respectively. After the four-step CFS data processing, we get a defect location map $\psi(x, y)$ as shown the last row. In (b), the map contains two terms that are centered at two potential defect locations, indicated by the two orange arrows, and is symmetric about the origin, leading to a two-fold ambiguity. (d) In model-based OAM CFS, the defect location map appears to be similar to that in the model-based CFS, however, these two terms have opposite handedness in phase. We thus can use this unique feature to break the ambiguity and determine the correct defect location, as indicated by the orange arrow. (e) In model-based Differential OAM CFS, the defect map again have two ambiguous terms. (f) In model-free Differential OAM CFS, the map shows four ambiguous terms. Using several symmetric axes and point, as well as the phase handedness, we can then determine the potential defect locations with just two ambiguous terms, as indicated by the two orange arrows. In (b, e, f), we can further use other constraints such as the scanning pattern to break the two-fold ambiguity and determine the final defect location. All figures are plotted with amplitude and phase being represented as brightness and hue, respectively. This figure is adopted from Ref. [12].

$$
\begin{aligned}
I_{q=0}(f_x, f_y) &= \left|\Im\{[S(x,y) + D(x,y)]P_{q=0}(x,y)\}\right|^2 \\
&= \left|\Im\{S(x,y)P_{q=0}(x,y)\}\right|^2 + \left|\Im\{D(x,y)P_{q=0}(x,y)\}\right|^2 + \\
&\quad \Im\{S(x,y)P_{q=0}(x,y)\}\Im\{D(x,y)P_{q=0}(x,y)\}^* + \Im\{S(x,y)P_{q=0}(x,y)\}^*\Im\{D(x,y)P_{q=0}(x,y)\}, \quad (1)
\end{aligned}
$$

where * represents the complex conjugate and $\Im$ represents the Fourier transform operation. We model the light-matter interaction as a single scattering event and treat the propagation of light from the sample plane to the far-field detector plane using Fraunhofer diffraction. The corresponding reference diffraction pattern from the defect-free sample on the detector plane is $I_r(f_x, f_y) = \left|\Im\{S(x,y)P_{q=0}(x,y)\}\right|^2$, and the difference between the measured and reference pattern $\Psi(f_x, f_y)$ is:

$$
\begin{aligned}
\Psi(f_x, f_y) &= I_{q=0}(f_x, f_y) - I_r(f_x, f_y) \\
&= \left|\Im\{D(x,y)P_{q=0}(x,y)\}\right|^2
\end{aligned}
$$

$$+\Im\{S(x,y)P_{q=0}(x,y)\}\Im\{D(x,y)P_{q=0}(x,y)\}^* + \Im\{S(x,y)P_{q=0}(x,y)\}^*\Im\{D(x,y)P_{q=0}(x,y)\}. \quad (2)$$

In the case where defects are minuscule in comparison to the beam size, the first term on the right-hand side of Eq. (2) is negligible, and the defect can be approximated by a δ function, *i.e.,* $D(x,y) = c\delta(x - x_0, y - y_0)$, where c is a complex scaling factor and (x_0, y_0) is the coordinate of the defect. The inverse Fourier transform of Eq. (2) yields the defect location map $\psi(x,y)$ as follows:

$$\begin{aligned}\psi(x,y) &= \Im^{-1}\{\Psi(f_x, f_y)\} \\ &= c^* S(x + x_0, y + y_0)P_{q=0}(x + x_0, y + y_0)P_{q=0}(x_0, y_0)^* \\ &\quad + cS(-x + x_0, -y + y_0)^* P_{q=0}(-x + x_0, -y + y_0)^* P_{q=0}(x_0, y_0). \end{aligned} \quad (3)$$

The first term in Eq. (3) is proportional to the field from the defect-free sample, $S(x,y) \cdot P_{q=0}(x,y)$, shifted by $(-x_0, -y_0)$, and the second one is proportional to the complex conjugate of $S(x,y) \cdot P_{q=0}(x,y)$, rotated by 180° and shifted by (x_0, y_0). Since these two terms are centered at the defect location, (x_0, y_0), and its mirror location about the origin, $(-x_0, -y_0)$, their centroids are possible locations of the defect. Consequently, there is an inherent two-fold ambiguity in the determined defect location.

Figure 2 shows the CFS data recording and processing flow for both Gaussian and OAM beam based CFS. For model-based Gaussian CFS (the first column of Fig. 2), a Gaussian beam illuminating a uniform sample with a point defect (the white dot pointed by the red arrow) is shown in Fig. 2(a). All subfigures, including those on the sample plane and the defect location maps, are plotted with amplitude and phase being represented as brightness and hue, respectively. The 4-step data recording and processing flow include:

(1) Illuminate the sample with a Gaussian beam,
(2) Record a far-field diffraction pattern,
(3) Subtract the recorded pattern from the reference pattern,
(4) Inverse Fourier transform the difference.

We then obtain the defect location map $\psi(x,y)$ as shown in Fig. 2(b), which contains the two ambiguous terms introduced in Eq. (3), and shows the two possible defect locations, as indicated by the orange arrows.

2.2 Model-based CFS using an OAM beam

In the model-based OAM CFS, we use an OAM beam with an OAM value of q to replace the Gaussian beam as the illumination, as shown in Fig. 1(b). Because of its intrinsic spiral phase structure, the OAM beam will break the symmetry in diffraction patterns $I_q(f_x, f_y)$, which can be leveraged to perform sensitive defect inspection. Note that Eqs. (1-3) are general mathematical expressions, regardless of the illumination. Figure 2(c) shows an OAM beam with $q = +1$ incident onto a uniform sample with a point defect (the white dot indicated by the red arrow). After performing a similar 4-step data recording and processing as described in the previous subsection 2.1, we get the defect location map $\psi(x,y)$ shown in Fig. 2(d). The map appears to have the same features as in Fig. 2(b), but the two ambiguous terms have opposite handedness in phase. Therefore, the two-fold ambiguity is broken, and the correct defect location is determined. As indicated in Eq. (3) and by the orange arrow in Fig. 2(d), the center of the component that has the opposite handedness to that of the OAM beam indicates the correct defect location.

To better understand the benefits of using OAM beams, we develop an intuition for why OAM beams cause symmetry breaking in diffraction patterns by comparing the characteristics of diffraction patterns from Gaussian and OAM CFS. We consider a uniform substrate with a small additive amplitude-only defect, which can be expressed as $D(x,y) = r\delta(x - x_0, y - y_0)$, where r is the defect amplitude and (x_0, y_0) is the location of the defect on the sample plane. The defect amplitude here means the magnitude of the normalized complex reflectivity or transmissivity of the defect in reflection or transmission geometries, respectively, and thus r varies between 0 and 1. The sample is illuminated by a coherent Gaussian or OAM beam, $P_q(x,y)$, while the point defect is assumed to be located to the right of the beam for the discussion. The far-field diffraction pattern is written in Eq. (1). The first and second terms on the right-hand side of Eq. (1) are the intensity distribution of the complex electromagnetic fields resulting from the defect-free substrate and the defect, *i.e.,* $\Im\{S(x,y)P_q(x,y)\}$ and $\Im\{D(x,y)P_q(x,y)\}$, which we will refer to as the substrate field and defect field, respectively. The third and fourth terms denote the interference intensity pattern between the substrate and defect fields, which is real-valued, and we will refer to it as the "interference intensity pattern". Figure 3 shows these fields individually for both Gaussian and OAM CFS. The simulated Gaussian and OAM beams are set such that their peak intensity and integrated power are both the same.

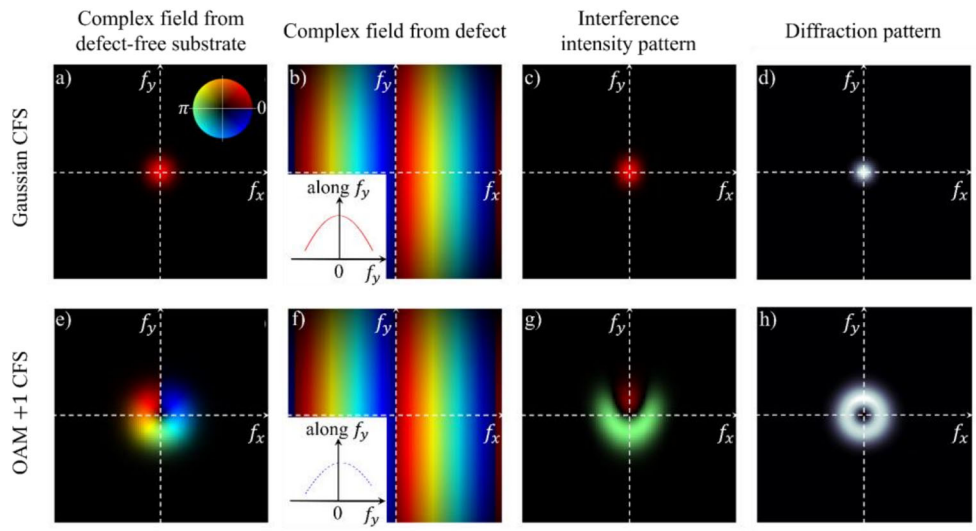

Fig. 3. The characteristics of far-field diffraction patterns from Gaussian and OAM beams illuminating on blank substrate with amplitude-only defects. (a) and (b) show the complex fields from the defect-free substrate and from the defect, *i.e.,* $\Im\{S(x,y)P_q(x,y)\}$ and $\Im\{D(x,y)P_q(x,y)\}$ in Eq. (1), in the far-field from Gaussian CFS. The defect is assumed to be located to the right of the beam for the discussion. The inset of (b) shows the amplitude of the defect field for Gaussian CFS along f_y axis and it is symmetric. (c) shows the interference intensity pattern, i.e. $\Im\{S(x,y)P_{q=0}(x,y)\}\Im\{D(x,y)P_{q=0}(x,y)\}^* + \Im\{S(x,y)P_{q=0}(x,y)\}^*\Im\{D(x,y)P_{q=0}(x,y)\}$, and (d) shows the far-field diffraction pattern, which is the summation of intensity of the substrate and defect fields, and the interference intensity pattern. Similar plots for OAM ± 1 CFS are shown in (e-h). The inset of (f) shows the amplitude of the complex field from defect for OAM CFS along f_y axis, and it is not symmetric because of the spiral phase of OAM beams. The interference intensity pattern of OAM CFS in (g) shows significant asymmetry due to the spiral phase of the OAM beam. This asymmetry further propagates into the far-field diffraction pattern, as shown in (h). The color wheel for complex field representation is shown in the top right corner of (a), where amplitude and phase are represented by brightness and hue, respectively. This figure is adopted from Ref. [12].

For a Gaussian beam at focus, *i.e.,* with a flat wavefront, the complex substrate and defect fields are shown in Fig. 3(a) and 3(b). The horizontal linear phase in Fig. 3(b) is caused by the shift of the defect to the right in real space relative to the center of the illumination beam. Figure 3(c) shows the interference intensity pattern, which is real-valued and symmetric. The final far-field diffraction pattern is the summation of the intensity of substrate and defect fields and the interference intensity pattern, which is shown in Fig. 3(d). Similarly, the complex substrate and defect fields, the interference intensity pattern, and the far-field diffraction pattern from the OAM beam at focus with $q = +1$ are shown in Fig. 3(e-h). As clearly shown in the inset of Fig. 3(f), the defect field is not centered in f_y direction. This is because the small defect sees the local spiral phase from the OAM beam approximately as a linear phase — consequently, in frequency space, the field is shifted away from the center according to the Fourier shift theorem. Moreover, the interference intensity pattern, shown in Fig. 3(g), shows significant asymmetry in the vertical direction. It is locally linear, while the globally spiral phase of the OAM beams that result in the asymmetry in the complex defect field and the interference intensity pattern, thus causing significant asymmetry in diffraction patterns as shown in Fig. 3(h).

In fact, the amplitude and phase of defect have different effects on the defect field and interference intensity pattern: the defect amplitude scales only the amplitude, *i.e.,* the overall brightness, of the defect field, while the defect's phase shifts the phase of the defect field. For small-sized amplitude-only defects on blank planar substrates, when illuminated by a Gaussian beam at focus, the substrate field has a Gaussian amplitude distribution with a nearly flat phase, while the defect field has close to uniform amplitude distribution with a linear phase in an area where the substrate field has significant amplitude. The linear phase is caused by the shift of the defect relative to the beam center. The substrate and defect fields are in-phase around the origin of (f_x, f_y) space, and the interference intensity pattern is symmetric about both f_x and f_y, see Fig. 3(a-c). Moreover, any change in defect amplitude scales the amplitude of the defect field and interference intensity pattern but does not change their patterns. Consequently, Gaussian beams at focus illuminating blank planar substrates

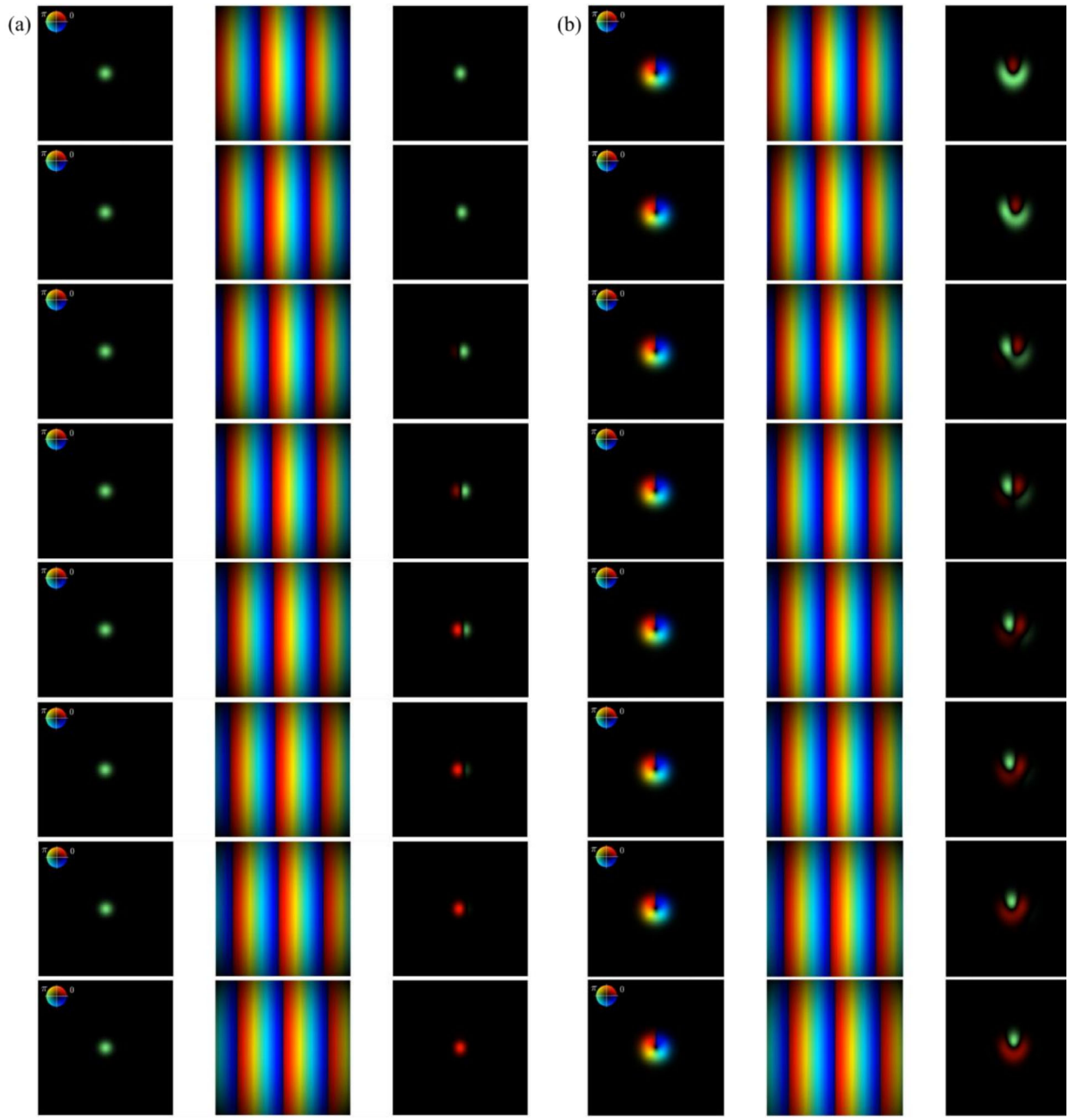

Fig. 4. The substrate and defect fields and interference intensity patterns from Gaussian (a) and OAM beams (b) illuminating on blank substrate with phase-only defects. (a) The three columns show the complex substrate fields (left), the complex defect fields (middle) and the interference intensity patterns (right) from a Gaussian beam. The rows correspond to varying relative phase between substrate and defect, *i.e.*, 0, 0.2π, 0.4π, 0.5π, 0.6π, 0.7π, 0.8π and π from the first to the last row. Similarly, (b) shows substrate fields (left), the complex defect fields (middle) and the interference intensity patterns (right) but with an OAM beam. The color wheel for complex field representation is shown in the top right corner, where amplitude and phase are represented by brightness and hue, respectively.

with amplitude-only defects do not result in an asymmetry in the far-field diffraction patterns. However, when illuminated by an OAM beam at focus, the defect field is the same, but the substrate field has a donut-shaped amplitude distribution with a spiral phase distribution, as shown in Fig. 3(d). They interfere constructively around the top half of the f_y axis, and destructively around the bottom half of the f_y axis, resulting in significant asymmetry, as shown in Fig. 3(g). Notice that if the Gaussian and OAM beams are out of focus, the additional quadratic phase will cause a very small increase in

asymmetry that is negligible compared to asymmetry from OAM beams. For simplicity, we will focus on the discussion about Gaussian and OAM beams at the focus.

For small-sized phase-only defects on blank planar substrates, when illuminated by a Gaussian beam at focus, the substrate field is the same as that shown in Fig. 3(a), but the phase of the defect field is shifted by the amount of the defect phase. As a result, the substrate and defect fields are in-phase away from the origin of (f_x, f_y) space, causing an asymmetry in the interference intensity pattern in the direction of the linear phase of the defect field. However, for OAM beams at focus, the interference of the donut-shaped substrate field and the phase-shifted defect field is much more complicated, especially for OAM beams with high q value. In our simulation, we scanned the defect phase from 0 to π and showed the change in the substrate and defect fields, and the interference intensity pattern in Fig. 4.

2.3 Model-based differential CFS using two OAM beams with opposite charges

OAM beams can have either positive or negative OAM, which makes differential measurements possible. When used in conjunction with a library of reference patterns, this technique will be referred to as model-based differential OAM CFS, and the setup is shown in Fig. 1(b). At each scan point, a sample under inspection is illuminated by two OAM beams with opposite charges, one at a time. The OAM beams can be expressed as $P_{q=\pm1}(x,y) = p(x,y)e^{\pm i\varphi(x,y)}$, where $p(x,y)$ and $\varphi(x,y)$ are the amplitude and phase profiles of the OAM beams, respectively. One far-field diffraction pattern is recorded for each illumination on the detector plane, $I_{q=\pm1}(f_x, f_y)$. One diffraction pattern is subtracted from the other to form a differential measurement, for example, $M(f_x, f_y) = I_{q=+1}(f_x, f_y) - I_{q=-1}(f_x, f_y)$, which is then compared with the corresponding reference pattern, $M_r(f_x, f_y)$, to detect defects. Using the same notation, the counterparts of Eq. (2), with the first negligible term being dropped, and Eq. (3) are:

$$\begin{aligned}\Psi(f_x, f_y) &= M(f_x, f_y) - M_r(f_x, f_y)\\ &= \Im\{S(x,y)P_{q=+1}(x,y)\}\Im\{D(x,y)P_{q=+1}(x,y)\}^*\\ &\quad - \Im\{S(x,y)P_{q=-1}(x,y)\}\Im\{D(x,y)P_{q=-1}(x,y)\}^*\\ &\quad + \Im\{S(x,y)P_{q=+1}(x,y)\}^*\Im\{D(x,y)P_{q=+1}(x,y)\}\\ &\quad - \Im\{S(x,y)P_{q=-1}(x,y)\}^*\Im\{D(x,y)P_{q=-1}(x,y)\},\end{aligned} \tag{4}$$

and

$$\begin{aligned}\psi(x,y) &= i2cS(x+x_0, y+y_0)p(x+x_0, y+y_0)sin[\varphi(x+x_0, y+y_0)]\\ &\quad -i2cS(-x+x_0, -y+y_0)^*p(-x+x_0, -y+y_0)sin[\varphi(-x+x_0, -y+y_0)].\end{aligned} \tag{5}$$

The sine terms in Eq. (5) originate from the subtraction of the two OAM beams with an opposite charge, *i.e.,* $e^{i\varphi(x,y)} - e^{-i\varphi(x,y)}$. It consists of the following two components: $S(x,y)p(x,y)sin\varphi(x,y)$ shifted by $(-x_0, -y_0)$ and its complex conjugate rotated by 180° and shifted by (x_0, y_0), which are shown in Fig. 2(e). Similarly, since these two terms are centered at the correct defect location and its symmetric point about the origin, the correct defect location can be then determined with a two-fold ambiguity, as indicated by the two orange arrows in Fig. 2(e).

2.4 Model-free differential CFS using two OAM beams with opposite charges

All CFS methods discussed so far require a library of reference patterns. However, in a special case where the defect-free sample should have a reflection symmetry, the need for a library can be eliminated. This technique is referred to as model-free differential OAM CFS and its schematic is also shown in Fig. 1(b). Without loss of generality, we can define the real space coordinate such that one of these symmetric axes is on the y-axis, *i.e.,* $S(-x,y) = S(x,y)$. Similar to the model-based differential OAM CFS, at each scan position, the sample under inspection is illuminated twice by two OAM beams with opposite charges, and then a far-field diffraction pattern is recorded for each illumination. Importantly, one diffraction pattern, for example $I_{q=-1}(f_x, f_y)$, is first *flipped* around f_y-axis on the detector plane, which is the reciprocal-space counterpart of the y-axis. Then, the flipped diffraction pattern $I_{q=-1}(-f_x, f_y)$ is subtracted from the other diffraction pattern $I_{q=+1}(f_x, f_y)$ to get the differential measurement, $I_{q=+1}(f_x, f_y) - I_{q=-1}(-f_x, f_y)$. Using the same notation, the counterparts of Eq. (3) is:

$$\begin{aligned}\Psi(f_x, f_y) &= \Im\{S(x,y)P_{q=+1}(x,y)\}\Im\{D(x,y)P_{q=+1}(x,y)\}^*\\ &\quad -\Im\{S(x,y)P_{q=+1}(x,y)\}\Im\{D(-x,y)P_{q=+1}(x,y)\}^*\\ &\quad +\Im\{S(x,y)P_{q=+1}(x,y)\}^*\Im\{D(x,y)P_{q=+1}(x,y)\}\\ &\quad -\Im\{S(x,y)P_{q=+1}(x,y)\}^*\Im\{D(-x,y)P_{q=+1}(x,y)\}.\end{aligned} \tag{6}$$

A model-free method is made possible because the reflection symmetry between the two OAM beams with opposite charges, $P_{q=+1}(-x,y) = P_{q=-1}(x,y)$, is the same as that of the sample, $S(-x,y) = S(x,y)$. Consequently, it is necessary that the beam center is scanned along with one of the axes of the reflection symmetry of the defect-free sample. Considering one-dimensional grating samples, for example, the beam center should be scanned either perpendicular to the grating lines, or parallel to the grating lines along the center of grating lines or grooves. The former scanning scheme is easier to achieve in real experiments. To derive Eq. (6), first of all, exploiting the symmetry properties of $S(x,y)$ and $P_{q=\pm1}(x,y)$ leads to the cancellation of the first terms of $I_{q=\pm1}(f_x,f_y)$, i.e., $\left|\Im\{S(x,y)P_{q=-1}(x,y)\}\right|^2 - \left|\Im\{S(-x,y)P_{q=+1}(-x,y)\}\right|^2 = 0$. Secondly, the second term in Eq. (1) for $q = \pm1$ OAM beams, $\left|\Im\{D(x,y)P_{q=\pm1}(x,y)\}\right|^2$, is negligible because it is many orders of magnitude smaller than other terms. Furthermore, if the defect is small enough in comparison to the beam size that it can be approximated as a δ-function, i.e., $D(x,y) = \delta(x-x_0, y-y_0)$, where (x_0, y_0) is the position of the defect, an inverse Fourier transform of $\Psi(f_x,f_y)$ yields:

$$\begin{aligned}\psi(x,y) = {} & cS(x+x_0,y+y_0)P_{q=+1}(x+x_0,y+y_0)P_{q=+1}(x_0,y_0)^* \\ & -cS(x-x_0,y+y_0)P_{q=+1}(x-x_0,y+y_0)P_{q=+1}(-x_0,y_0)^* \\ & +c^*S(-x+x_0,-y+y_0)^*P_{q=+1}(-x+x_0,-y+y_0)^*P_{q=+1}(x_0,y_0) \\ & -c^*S(-x-x_0,-y+y_0)^*P_{q=+1}(-x-x_0,-y+y_0)^*P_{q=+1}(-x_0,y_0). \end{aligned} \tag{7}$$

Equation 7 consists of the following four terms: (1) the positive OAM beam incident onto the defect-free sample, $S(x,y)P_{q=+1}(x,y)$, shifted by $(-x_0,-y_0)$; (2) $S(x,y)P_{q=+1}(x,y)$ shifted by $(x_0,-y_0)$; (3) the complex conjugate of $S(x,y)P_{q=+1}(x,y)$, rotated by 180° and shifted by (x_0,y_0); and (4) the complex conjugate of $S(x,y)P_{q=+1}(x,y)$, rotated by 180°180 and shifted by $(-x_0,y_0)$. Figure 2(f) shows the corresponding defect location map $\psi(x,y)$, which contains the four components introduced above. Since they are centered at $(\pm x_0, \pm y_0)$, one can figure out the defect location from $\psi(x,y)$ with a four-fold ambiguity. Furthermore, as indicated by Eq. (7) and shown in Fig. 2(f), the phase of the term that centers at the defect location has the same handedness as the negative OAM beam if the differential measurement is performed with $M(f_x,f_y) = I_{q=+1}(f_x,f_y) - I_{q=-1}(-f_x,f_y)$, which decreases the ambiguity to two-fold. It is straightforward to show that if the differential measurement is performed as $M(f_x,f_y) = I_{q=-1}(f_x,f_y) - I_{q=+1}(-f_x,f_y)$, the phase of the component which centers at the defect location has the same handedness as the positive OAM beam.

3. SIMULATIONS AND DISCUSSIONS

In this section, we first numerically simulate three CFS techniques on uniform samples with point defects, including (1) model-based Gaussian CFS, (2) model-based OAM CFS and (3) model-free differential OAM CFS, and compared the sensitivity of these techniques in detection of the presence of defects. Once defects are detected using the methods discussed in subsection 3.1, one can then take an inverse Fourier transform of $\Psi(f_x,f_y)$ to further locate the defects. Since the sample discussed in this section is symmetric about x and y axes, the model-free differential OAM CFS is be applied to perform defect detection, and the model-based differential OAM CFS is not discussed here. However, in cases where defect-free samples do not have reflection symmetry, the model-based differential OAM CFS may be used, since the model-free differential OAM CFS does not work.

3.1 Defect detection based on asymmetric far-field diffraction patterns

In this section, we propose two methods to detect asymmetric far-field diffraction patterns from defects. The first method uses quadrant detectors (*QD*s), where we found that using OAM beams is advantageous over the conventional Gaussian CFS, leading to higher *QD* signal and thus higher sensitivity. The second method is based on 2D image sensors, such as cameras (*CAM*s), and is suitable for all CFS techniques, including both model-based and model-free differential OAM CFS. Although slower for data acquisition and processing speed, the camera-based method provides even higher sensitivity in defect detection. As a proof-of-concept demonstration, we limit our simulations and discussion on additive defects on a planar substrate and 1D gratings. The size of the defect is set to be $0.02w_0$, where w_0 is the waist radius of the Gaussian beam. In the case of inspecting a planar substrate, the illumination beam, indicated by the black dashed circle in the inset (2) of Fig. 5(a), is scanned in a 2D raster pattern across the sample under inspection. The green dashed lines denote two consecutive scan lines.

The use of *QD*s has been demonstrated to detect asymmetry in far-field diffraction patterns in Gaussian CFS, which can enhance SNR by almost two orders of magnitude [2]. To implement this method, we center far-field diffraction patterns on a detector, either by dividing a 2D image from a camera into four equal quadrants or by collecting scattered light into a quadrant photodiode. As shown in the inset (1) in Fig. 5(a), we can then calculate the horizontal asymmetry ($QD_{L\text{-}R}$) of the total number of photons between left and right quadrants, and vertical asymmetry ($QD_{T\text{-}B}$) between the top and bottom quadrants, which are defined as:

$$\begin{cases} QD_{L-R} = \sum_{Q1,Q3} \Psi(f_x, f_y) - \sum_{Q2,Q4} \Psi(f_x, f_y) = \sum_{f_x<0, f_y} \left(\Psi(f_x, f_y) - \Psi(-f_x, f_y) \right), \\ QD_{T-B} = \sum_{Q1,Q2} \Psi(f_x, f_y) - \sum_{Q3,Q4} \Psi(f_x, f_y) = \sum_{f_x, f_y>0} \left(\Psi(f_x, f_y) - \Psi(f_x, -f_y) \right). \end{cases} \tag{8}$$

In general, for model-based Gaussian and OAM CFS, $\Psi(f_x, f_y)$ is the difference between measured and reference patterns and is defined in Eq. (2). Specifically, for uniform planar substrates, since the reference pattern is symmetric in both f_x and f_y directions, $\Psi(f_x, f_y)$ can be replaced by the measured diffraction pattern.

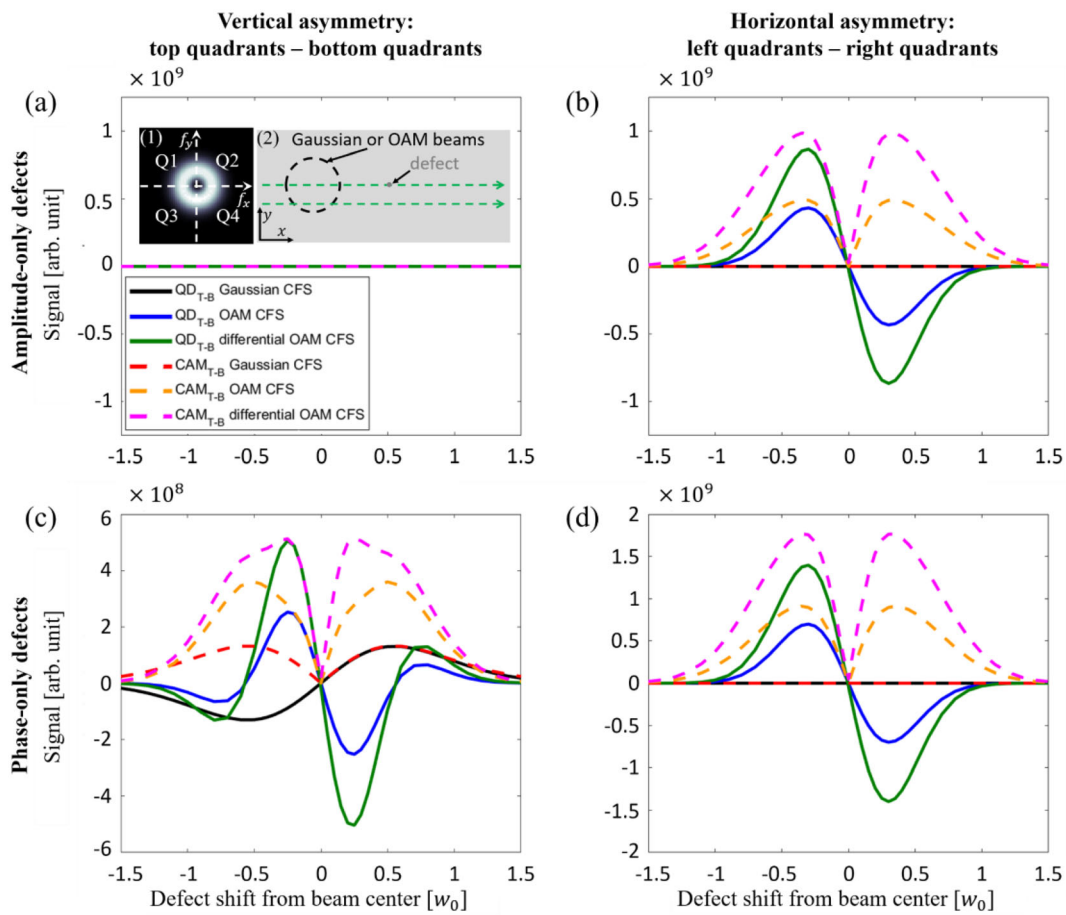

Fig. 5. CFS signals from asymmetric far-field diffraction patterns in Gaussian CFS, OAM CFS and differential OAM CFS due to the presence of defects, detected by quadrant detectors (*QDs*) or a camera (*CAM*). (a, b) Given an amplitude-only defect with $r = 0$, the vertical asymmetry signals (QD_{T-B} and CAM_{T-B}) are shown in solid and dashed lines in (a), and horizontal asymmetry signals (QD_{L-R} and CAM_{L-R}) are shown in solid and dashed lines in (b). The defect size is set to be $0.02w_0$, where w_0 is waist radius of the Gaussian beam, and the defect shift from beam center is normalized to w_0. We also varied r from 0 to 0.7 in steps of 0.1 and made a series of plots showing QD signals (see Fig. 6(a)). (c, d) Given a phase-only defect with $\phi_0 = 135°$, the vertical and horizontal asymmetry signals are show in (c) and (d), respectively. Notice that Gaussian CFS has no sensitivity to amplitude-only defects, while OAM beams have high sensitivity. Furthermore, differential OAM CFS has twice as much signal as single OAM CFS. Lastly, CAM signals are higher than QD signals. Inset (1) of (a) shows an example far-field diffraction pattern, grouped into four equal quadrants, Q1, Q2, Q3, and Q4, of an OAM $q = +1$ beam illuminating a planar substrate with a point defect. Inset (2) shows the schematic of the scanning process for defect detection. The illumination is scanned over the sample in a 2D raster pattern, where the green dashed lines indicate two consecutive scan lines. A series of plots with varying ϕ_0 can be seen in Fig. 6(b). All subfigures share the legend shown in (a). This figure is adopted from Ref. [12].

The other approach to quantify the asymmetric diffraction patterns is the sum of the absolute value of the difference between left and right (or top and bottom) quadrants. This requires a 2D image sensor such as a camera and the signal can

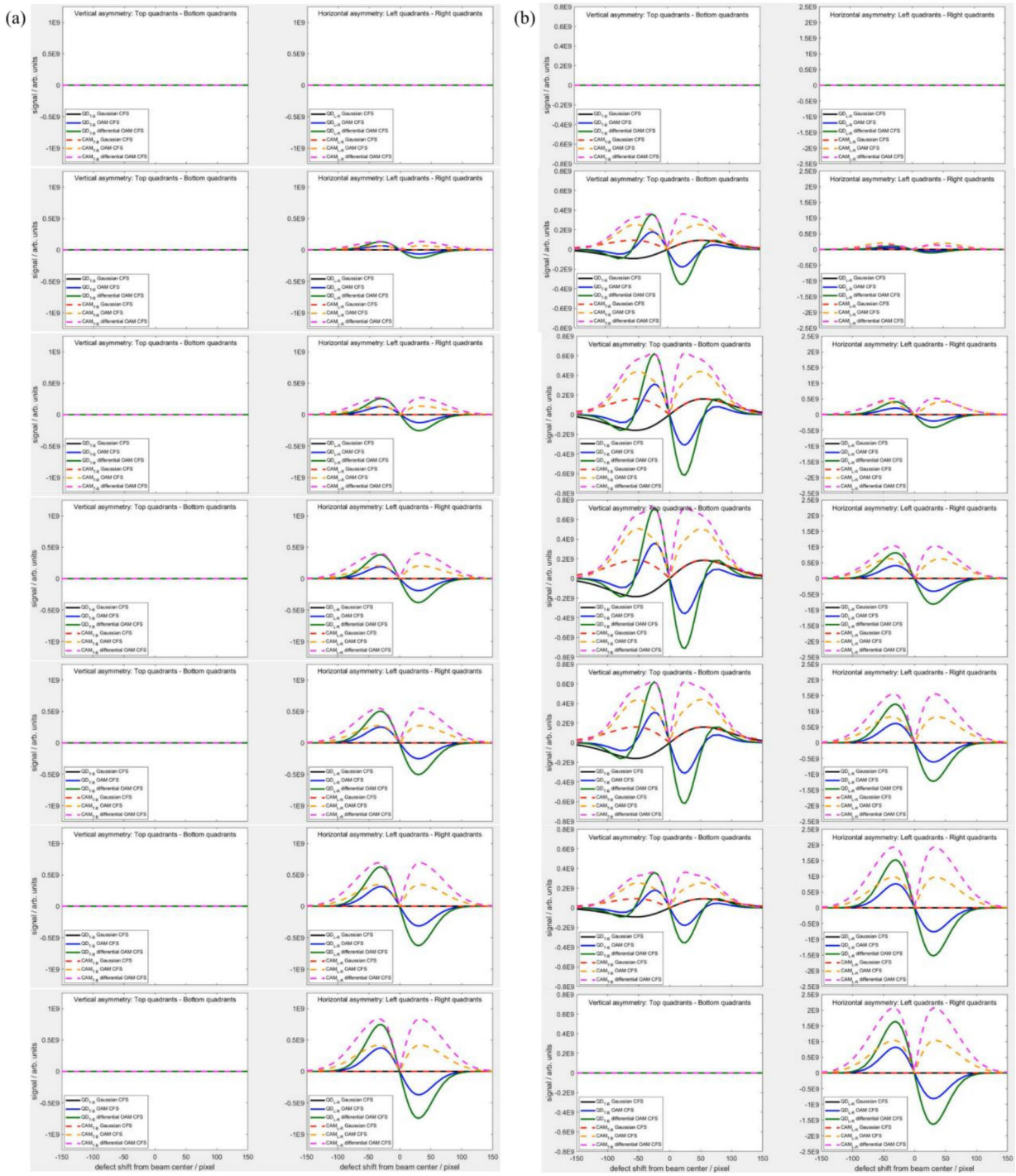

Fig. 6. Signals in Gaussian CFS, OAM CFS, and differential OAM CFS for amplitude-only defects (a) and phase-only defects (b). (a) The two columns show vertical asymmetry (left) and horizontal asymmetry (right) in far-field diffraction patterns in the presence of a small amplitude-only defect. The rows correspond to varying amplitude difference between substrate and defect ranging from 0 to 0.6 in steps of 0.1. (b) The two columns show vertical asymmetry (left) and horizontal asymmetry (right) in far-field diffraction patterns in the presence of a small phase-only defect. The rows correspond to varying phase difference between substrate and defect ranging from 0 to 180 degrees in steps of 30 degrees.

be defined as follows:

$$\begin{cases} CAM_{L-R} = \sum_{f_x<0,f_y} \left|\Psi(f_x,f_y) - \Psi(-f_x,f_y)\right|, \\ CAM_{T-B} = \sum_{f_x,f_y<0} \left|\Psi(f_x,f_y) - \Psi(f_x,-f_y)\right|. \end{cases} \tag{9}$$

The difference between Eq. (8) and Eq. (9) is the absolute value operation in the summand in Eq. (9). If we only consider Poisson noise, which is made possible by the state-of-the-art photon counting detector technology, the noise level of *QD* and *CAM* signals is the same given the noise in all pixels is independent and identically distributed, according to the propagation of uncertainty in statistics.

In our simulations, we investigated two types of defects, an amplitude-only defect and a phase-only defect. The substrate is set to be $S(x,y) = 0.7$ on the sample plane to model a partially reflecting flat surface. An amplitude-only defect is

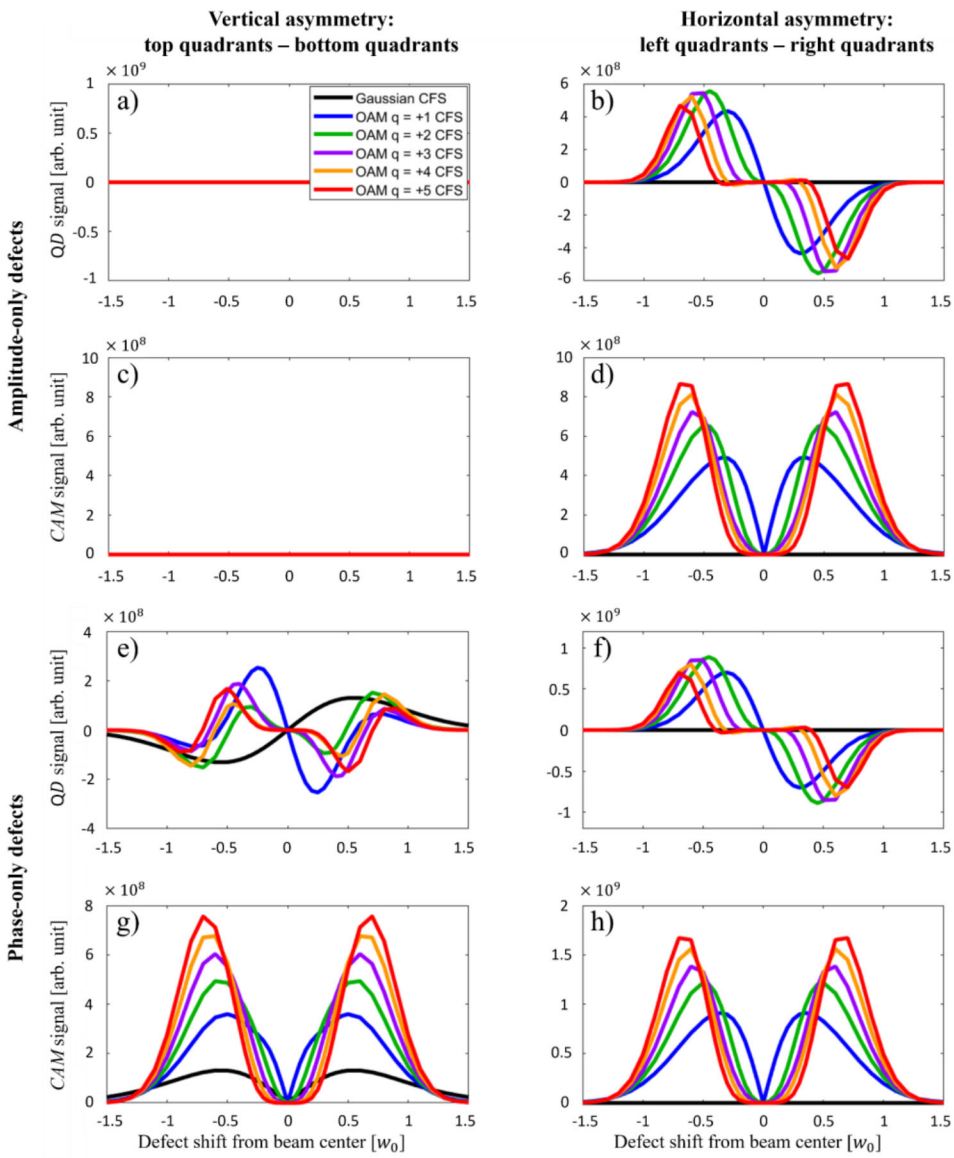

Fig. 7. Effect of varying OAM charges in both model-based Gaussian CFS and OAM CFS. Given an amplitude-only defect, (a, b) show the vertical and horizontal QD asymmetry signals (QD_{T-B} and QD_{L-R}) and (c, d) show the vertical and horizontal *CAM* asymmetry signals (CAM_{T-B} and CAM_{L-R}) for Gaussian and OAM beams with different charges. Given a phase-only defect, (e, f) show vertical and horizontal QD asymmetry signals and (g, h) show the vertical and horizontal *CAM* signals for Gaussian and OAM beams. All subfigures share the legend shown in (a). Note that the monotonic signal increases only occur in the camera-based method, while the signals will get maximized at particular OAM charges in the *QD*-based method. This figure is adopted from Ref. [12].

defined as $D(x,y) = r\,\delta(x - x_0, y - y_0)$ with r being the defect amplitude and (x_0, y_0) being the location of the defect on the sample plane, while a phase-only defect is defined as $D(x,y) = 0.7e^{i\phi_0}\,\delta(x - x_0, y - y_0)$ with ϕ_0 being the relative phase between the substrate and the defect. For an amplitude-only defect with $r = 0$, the vertical and horizontal *QD* signals from diffraction pattern asymmetries as a function of scan position normalized to the Gaussian beam waist radius w_0 are shown in Fig. 5(a) and 5(b). We also varied r from 0 to 0.7 in steps of 0.1 and made a series of plots showing *QD* signals (see Fig. 6(a)). Gaussian beams at focus have no sensitivity at all to amplitude-only defects because the diffraction patterns are perfectly symmetric, while OAM beams at focus are very sensitive due to the spiral phase structure. For a phase-only defect with $\phi_0 = 135°$, the vertical and horizontal *QD* signals are shown in Fig. 5(c) and 5(d) and a series of plots with varying ϕ_0 between 0 and 180 degrees in steps of 30 degrees can be seen in Fig. 6(b). Even though Gaussian beams are sensitive to phase-only defects, OAM beams generally have 2-10 times higher signal levels, a significant improvement. An obvious advantage of using quadrant photodiodes is the high-speed data acquisition and processing and thus high inspection throughput, at any wavelength from visible light to EUV.

The *QD*-based method only captures the difference in the total number of photons between different quadrants, instead of the photon distribution or diffraction patterns within each quadrant. As a result, the detailed, pixel-by-pixel information about the asymmetry is lost. To overcome this, we now investigate the camera-based method. The vertical and horizontal *CAM* signals of amplitude-only and phase-only defects are shown in Fig. 5(a-d). It is evident that the camera-based method can further improve the signal level, compared to the *QD*-based method, and provides even higher sensitivity in defect detection. However, for higher sensitivity, data acquisition and processing time will be longer. The speed limit could be relaxed and eventually overcome given the high-speed CMOS cameras readily available for visible light and just released commercially for EUV and soft x-ray wavelengths.

3.2 Effect of varying OAM charges on sensitivity

We also studied the effect of varying OAM charge q on *QD* and *CAM* signals in model-based Gaussian and OAM CFS. As shown in Fig. 7(b, e, f), when the OAM charge varies from $q = 0$ (Gaussian beams) to $q = +5$ the *QD* signals for both amplitude- and phase-only defects first increase and then decrease. We attribute this phenomenon to the fact that an OAM beam with larger q diverges faster and the interference between the sample and defect fields may change accordingly. On the other hand, the *CAM* signals increase monotonically by a factor of at least 5 as the OAM charge increases from 0 to 5 as shown in Fig. 7(d, g, h). Higher signal gain is expected if higher OAM charge beams are used. This also indicates that OAM beams with larger charges result in more asymmetry in photon distribution, but not necessarily in the total number of photons of each quadrant.

3.3 Generalization of OAM beam-based CFS to 1D gratings

So far, we have limited our discussion to uniform planar substrates with additive point defects. The types of samples that work under this framework are defined by the assumption made in Sections 2.3 and 2.4: the defect-free sample is symmetric about some axis. It follows that these techniques can be easily generalized to inspect more complex samples with reflection symmetry (see Fig. 8(g)), such as 1D and 2D gratings and aperiodic sets of lines that are widely used in photolithography in semiconductor manufacturing. To support this statement, we briefly investigate point defects on a 1D granting. We follow a similar analysis discussed in subsection 2.2.

Figure 8(a) shows the complex field from a defect-free 1D grating, and Fig. 8(b) shows a complex field from an amplitude-only defect, and Fig. 8(c) is the resulting interference intensity pattern. The defect size is $0.02w_0$, and it is located $0.43w_0$ away from the beam center, which is also where the OAM beam with $q = 1$ reaches maximum intensity. The horizontal linear phase in Fig. 8(b) is caused by the shift of the defect to the right in real space relative to the center of the illumination beam. Similarly, Fig. 8(d-f) shows these three plots from an OAM beam with $q = 1$ illuminating on the same sample. Clearly, the interference intensity pattern from a Gaussian beam shows little asymmetry in all three diffraction orders, while that from an OAM beam exhibits significant asymmetry in all diffraction orders. The results in Fig. 8 are presented the same way as those in Fig. 3. As in the case of planer substrates (Fig. 3), in this case with 1D gratings (Fig. 8), constructive interference between the substrate and defect fields occurs in the top half of the field where they are in phase, while destructive interference happens in the bottom half of the field where they are out of phase. As a result, we can exploit the same *QD* or *CAM* methods to detect the asymmetric patterns and identify the presence and the locations of these defects on 1D line gratings. Analysis of 2D grating samples can be accomplished in a similar manner.

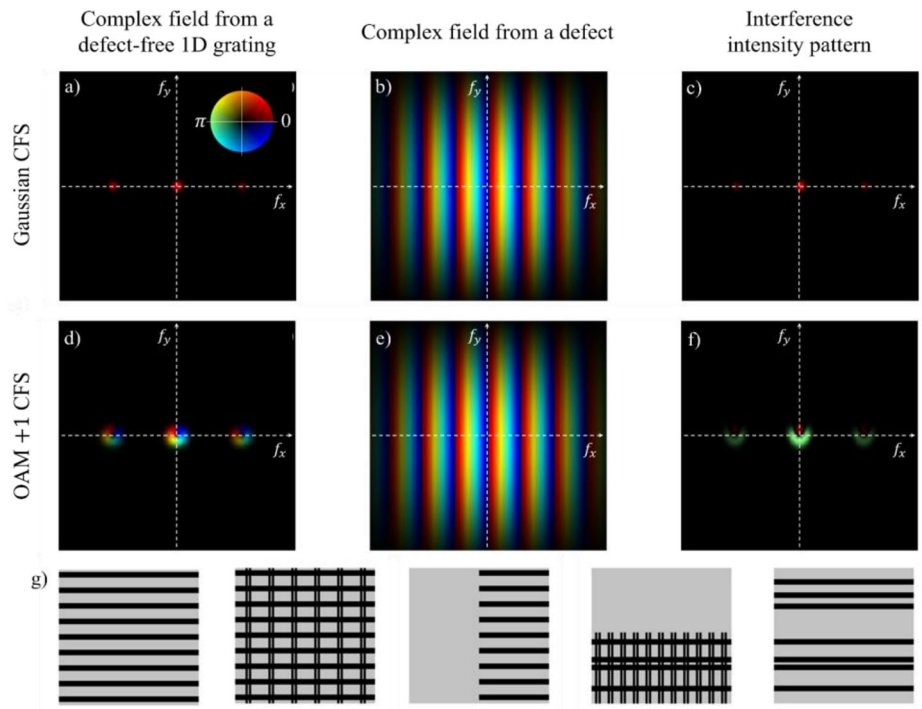

Fig. 8. The characteristics of far-field diffraction patterns resulting from Gaussian and OAM beam illumination of 1D line grating structures including amplitude-only defects. (a) and (b) show the complex field from the defect-free 1D grating and that from the defect, *i.e.,* $\Im\{S(x,y)P_q(x,y)\}$ and $\Im\{D(x,y)P_q(x,y)\}$ in Eq. (1), in the far-field from Gaussian CFS. The defect is assumed to be located to the right of the beam for the discussion. (c) shows the interference intensity pattern between sample and defect fields, i.e., $\Im\{S(x,y)P_{q=0}(x,y)\}\Im\{D(x,y)P_{q=0}(x,y)\}^* + \Im\{S(x,y)P_{q=0}(x,y)\}^*\Im\{D(x,y)P_{q=0}(x,y)\}$. Similar plots for OAM ± 1 CFS are shown in (d-f). The interference intensity pattern of OAM CFS in (f) shows significant asymmetry due to the spiral phase of the OAM beam. The color wheel for complex field representation is shown in the top right corner of (a), where amplitude and phase are represented by brightness and hue, respectively. (g) shows several example samples that can be inspected using any of the OAM CFS techniques presented here, including periodic 1D and 2D gratings, ends of these gratings and aperiodic set of lines. These example samples have reflection symmetry in at least one direction. This figure is adopted from Ref. [12].

3.4 Discussions and outlook

We now consider the effect of noise on our proposed CFS techniques. Common noise sources include shot noise, detector noises, sample noises (e.g., surface roughness), etc. One major challenge in defect detection on blank wafers is to distinguish between defect signals and the noise generated by pattern roughness, especially for dark-field CFS techniques. The dark-field CFS techniques block the specular reflection and capture the high-angle scattered light that in principle exists only in the presence of defects. However, the presence of surface roughness will also contribute to high-angle scattering, making it challenging to distinguish real defects from surface roughness. As for our proposed OAM-based CFS techniques, they are bright-field based and detect defects by measuring asymmetries in the far-field diffraction patterns. Because the above noise sources are mostly isotropic in the micrometer-size scale, they introduce limited asymmetries in the far-field diffraction patterns, thus making the proposed OAM-based bright-field CFS techniques very robust.

In numerical experiments, we focus on OAM CFS of uniform planar substrates and 1D gratings with additive point defects. However, we believe that this technique can be generalized easily to inspect more complex samples. Future efforts should be devoted to modeling light-matter interaction using more general theories, such as finite element methods or rigorous coupled-wave analysis [9,10], which can take complex 3D nanostructures or multiple scattering events into account if needed. Further evaluations on the impact of defects on printed patterns such as the actinic aerial image seen by photolithographic scanners are also needed, because the volumetric effects could lead to the "self-healing" of certain defects, reducing their printability. Furthermore, we anticipate the use of machine learning to help rapidly process OAM CFS diffraction patterns from different samples, as they are shown to be efficient and powerful tools for defect detection and classification [11]. We also envision the adaption of OAM beams or other structured beams for general purpose

scatterometry measurements beyond defect inspection such as grazing-incidence, small-angle, or wide-angle x-ray scattering.

4. CONCLUSION

In this paper, we presented OAM beam-based bright-field CFS techniques for high-sensitivity in-line defect detection. We numerically demonstrated the feasibility of such techniques by studying amplitude and phase point defects on planar substrates and 1D gratings. The OAM CFS technique outperforms conventional Gaussian CFS by up to an order of magnitude in SNR. Moreover, the differential OAM CFS technique using OAM beams with opposite OAM charges allows the model-free CFS, thus eliminating the need for a reference library, in cases where the defect-free sample has reflection symmetry. We also proposed to use two data acquisition and processing methods, the quadrant detector-based method works faster and is less computationally expensive, while the camera-based method has the potential to provide higher sensitivity. Our new techniques are general-purposed and are expected to be implemented as next-generation optical inspection tools. This could potentially address industrial metrology demands, such as mask, reticle, and wafer inspection, as the semiconductor industry marches toward sub-10 nm photolithography-based manufacturing.

ACKNOWLEDGEMENTS

The authors gratefully acknowledge support for this work by STROBE: A National Science Foundation Science & Technology Center, under Grant No. DMR 1548924. We also gratefully acknowledge support from DARPA W31P4Q-17-C-0104 and 140D0419C0094. Z. Z. acknowledges support by the China Scholarship Council Joint Doctoral Training Program, under Grant No. 201806260040.

REFERENCES

[1] Gawhary, O. E. and Petra, S. J. H., "Method and apparatus for determining structure parameters of microstructures," US Patent application 9,175,951B2 (11 March 2015).

[2] Roy, S., Assafrão, A. C., Pereira, S. F. and Urbach, H. P., "Coherent Fourier scatterometry for detection of nanometer-sized particles on a planar substrate surface," Opt. Express **22**(11), 13250-13262 (2014).

[3] Allen, L., Beijersbergen, M. W., Spreeuw, R. J. C. and Woerdman, J. P., "Orbital angular momentum of light and the transformation of Laguerre-Gaussian laser modes," Phys. Rev. A **45**, 8185-8189 (1992)

[4] Willner, A. E., Huang, H., Yan, Y., Ren, Y., Ahmed, N., Xie, G., Bao, C., Li, L., Cao, Y., Zhao, Z., Wang, J., Lavery, M. P. J., Tur, M., Ramachandran, S., Molisch, A. F., Ashrafi, N. and Ashrafi, S., "Optical communication using orbital angular momentum beams," Adv. Opt. Photonics **7**, 66-106 (2015).

[5] Torres, J. P. and Torner, L., *Twisted photons: applications of light with orbital angular momentum,* (John Wiley, 2011).

[6] Torner, L. and Torres, J. P., "Digital spiral imaging," Opt. Express **13**(3) 873-881 (2005).

[7] Peterhansel, S., Godecke, M. L., Paz, V. F., Frenner, K. and Osten, W., "Detection of overlay error in double patterning gratings using phase-structured illumination," Opt. Express **23**(19) 24246-24256 (2015).

[8] Peterhansel, S., Godecke, M. L., Frenner, K. and Osten, W., "Phase-structured illumination as a tool to detect nanometer asymmetry," J. Micro/Nanolith. MEMS MOEMS **15**(4) 044005 (2016).

[9] Moharam, M. G. and Gaylord, T. K., "Rigorous coupled-wave analysis of planar-grating diffraction," J. Opt. Sco. Am. **71**(7), 811-818 (1981).

[10] Wei, X., Wachters, A. J. H. and Urbach, H. P., "Finite-element model for three-dimensional optical scattering problems," J. Opt. Sco. Am. A **24**(3) 866-881 (2007).

[11] Kolenvo, D. and Pereira, S. F., "Machine learning techniques applied for the detection of nanoparticles on surfaces using coherent Fourier scatterometry", Opt. Express **28**(13), 19163-19186 (2020).

[12] Wang, B., Tanksalvala, M., Zhang, Z., Esashi, Y., Jenkins, N., Kapteyn, H., Murnane, M. and Liao, C.-T., "Coherent Fourier scatterometry using orbital angular momentum beams for defect detection", Opt. Express 29(3), 3342-3358 (2021)